Supporting Information for

Self-assembled supramolecular materials based on ruthenium(II) complexes with exceptional optical and photothermal properties

Xufeng Mai[a#], Jun Li[a#], Mengting Xie[a#], Xiaoyue Wang[a], Ming Sun[a], Ying Wu[a,b,c], Huijuan Yu[a,b]*, Lin Yu[a,b]*

---

[a]School of Chemical Engineering and Light Industry, Guangdong University of Technology, Guangzhou 510006, PR China
E-mail: xiaoheiyu79@gdut.edu.cn (Huijuan Yu), gych@gdut.edu.cn (Lin Yu).
[b]Guangdong Provincial Laboratory of Chemistry and Fine Chemical Engineering Jieyang Center, Jieyang 515200, China
[c]School of Chemistry and Chemical Engineering, South China University of Technology, Guangzhou, Guangdong, 510641, P. R. China.
[#]These authors contributed equally to this work

Table of Contents

1. Supporting Methods

2. Figures and Legends

1. Supporting Methods

1.1 General materials and methods

Unless otherwise specified, all reagents and solvents were obtained from commercial sources and used without further purification. 1,10-phenanthroline, 1,10-phenanthroline-5,6-dione, terephthalic aldehyde, 3,3'-diaminobenzidine, and ruthenium trichloride were purchased from Shanghai Aladdin Biochemical Technology Co. The ligand **bipb** and **bdppz**, and complex **Ru-bipb-2**，**Ru-bdppz-2** and Ru(phen)Cl_4 were prepared according to corresponding literature method [1-3].

MALDI-TOF-MS were recorded using a Bruker Ultraflextreme MALDI-TOF/TOF mass spectrometer. ESI-MS were analyzed using a Thermo Scientific TSQ Endura Triple Quadrupole Mass Spectrometer. ^1H NMR spectra were recorded on a Bruker AVANCE III HD 400 spectrometer, and all chemical shifts were given relative to tetramethylsilane (TMS). Element analysis was performed on an Elementar UNICUBE element analyzer. Transmission electron microscopy (TEM) images were recorded on a JME-2100 transmission electron microscope from JEOL Ltd. The powder X-ray diffraction data were recorded on a Bruker D8 ADVANCE diffractometers using a Cu Kα radiation (λ = 0.15416 nm). The composition and chemical shifts of elements on the sample surface were detected by X-ray photoelectron spectroscopy (XPS, Escalab 250Xi). Thermogravimetric analyses (TGA) were performed on a Perkin Elmer TGA4000 thermal gravimetric analyzer under N_2 atmosphere with a heating rate of 10 ^oC/min. UV-vis-NIR spectra were recorded on a UV-3600 plus spectrophotometer manufactured by Shimadzu. Emission spectra were recorded on a HORIBA Fluorolog-3 fluorescence spectrophotometer at room temperature. Emission lifetime spectra were recorded on an FLS920 spectrophotometer (EDINBURGH INSTRUMENTS LTD) at room temperature. Electron paramagnetic resonance spectra were measured using Bruke EMXplus-10/12 electron paramagnetic resonance spectrometer. Pump-probe transient absorption spectra were recorded on an LKS80 Laser Flash Photolysis Spectrometer (Applied Photophysics Ltd) with light excitation at 355 nm. Photothermal measurements were performed by using an 808-nm Fiber Coupled

Laser (Model: LDD, Xi'an Herschel Radiant Laser Technology Co. Ltd.), and the temperature response of the sample was measured with an IR thermal camera (Model:HT-A8, Xinsite Co. Ltd.).

1.2 The absorption of solid powders

Preparation of testing samples: Take approximately 250 mg of $BaSO_4$ (as a blank reference) and press it into a tablet. Then, thoroughly grind the solid sample powder, take 1-2 mg of the sample, and evenly spread it at the center of the $BaSO_4$ tablet. Use a stream of N_2 gas to blow away excess powder to avoid contamination of the integrating sphere.

Instrument and testing conditions: A solid-state UV-Vis-NIR spectrophotometer (SolidSpec-UV3700i) manufactured by Shimadzu was used. During the test, an integrating sphere detector was employed for light absorption measurement. The wavelength scanning range was from 220 to 2500 nm, with a medium scanning speed and a scanning interval of 1 nm.

1.3 Photothermal Conversion Efficiency

The photothermal conversion efficiency of the sample was determined according to the previous method[4-6]. Details are as follows:

Based on the total energy balance for this system:

$$\sum_i m_i, C_{p,\,i} \frac{dT}{dt} = Q_s - Q_{loss}$$

Where m_i (1.0 g) and $C_{p,i}$ (4.18 J/g.°C) are the mass and heat capacity of system components, respectively. Q_s is the photothermal heat energy input by irradiating NIR laser to cocrystal samples, and Q_{loss} is thermal energy lost to the surroundings. When the temperature is maximum, the system is in balance.

$$Q_s = Q_{loss} = hS\Delta T_{max}$$

Where h is the heat transfer coefficient, S is the surface area of the container, ΔT_{max} is the maximum temperature change.

The photothermal conversion efficiency η is calculated from the following equation:

$$\eta = \frac{hS\Delta T_{mas}}{I(1 - 10^{-A_{808}})}$$

Where I is the laser power (1.5 W/cm^2) and A_{808} is the absorbance of the samples at the wavelength of 808 nm (1.330).

In order to get the hS, a dimensionless driving force temperature, ϑ is introduced as follows:

$$\theta = \frac{T - T_{surr}}{T_{max} - T_{surr}}$$

Where T is the temperature of the sample, T_{max} is the maximum system temperature (62 °C), and T_{surr} is the initial temperature (29 °C).

And a sample system time constant τ_s

$$\tau_s = \frac{\sum_i m_i, C_{p,i}}{hS}$$

$$\frac{d\theta}{dt} = \frac{1}{\tau} \frac{Q_S}{hS\Delta T_{max}} - \frac{\theta}{\tau_s}$$

When the laser is off, $Q_s = 0$, therefore:

$$\frac{d\theta}{dt} = - \frac{\theta}{\tau_s}, \ t = - \tau_s ln\theta$$

So hS could be calculated from the slope of cooling time vs $ln\vartheta$. Therefore, τ_s is 117 s (**Figure S22b**). And the photothermal conversion efficiency η is 79.9%.

1.4 Simulation details

The kinetic energy of the monomers and multimers was computed using Forcite module in Materials Studio 7.0 . Specifically，molecule dynamic with NVE ensemble in 298 K was modeled, in which 1.0 fs time step and 30 ps of total time (i.e. $3x10^4$ steps) was simulated to capture the kinetic energy changes of these molecules. The initial velocities were random, and the integration tolerance was set to $5x10^4$ kcal/mol including velocities. The Van der Waals interactions between atoms were described using universal force field, while the electrostatic interactions were modeled using partial changes of atoms calculated using QEq method. HOMO and LUMO were computed using DFT (Density Functional Theory) in Gaussian 16, in which B3LYP level of theory with 6-31G(d)/LANL2DZ basis set was used, while octupole multipolar expansion and restricted Spin polarization were set. SCF density convergence was set to $1x10^{-8}$.

1.5 Synthesis procedure

Synthesis of 1,4-bis(1H-imidazo[4,5-f][1,10]phenanthrolin-2-yl)benzene (bipb) [2]

A mixture of 10-phenanthroline-5,6-dione (1.89 g, 9 mmol), ammonium acetate (13.86g, 180 mmol), terephthalic aldehyde (0.60 g, 4.5 mmol) and glacial acetic acid (150 mL) was refluxed for 3 h, then cooled to room temperature. An orange precipitate was obtained by filtration, then washed three times with deionized water and ethanol and dried under vacuum. (1.32g, 57.4%). MALDI-MS: m/z= 515.12 ($[M+H]^+$).

Synthesis of 11,11'-bidipyrido[3,2-a:2',3'-c]phenazine (bdppz) [3]

A mixture of 1,10-phenanthroline-5,6-dione (0.42 g, 2 mmol) and 3,3'-diaminobenzidine (0.214 g, 1 mmol) was refluxed in methanol (30 mL) for 8 h. During this period a yellow microcrystalline compound was separated from the solution. The compound was isolated by filtration, washed with hot methanol and chloroform, and dried under vacuum Yield: 0.48 g (85%). MALDI-MS: m/z= 563.10 ([M+H]$^+$).

Synthesis of [Ru$_2$(phen)$_4$(bipb)](PF$_6$)$_4$ (Ru-bipb-2) [2]

A solution of Ru(phen)$_2$Cl$_2$.2H$_2$O (0.284 g, 0.5 mmol) in glycerol was heated under nitrogen for 30 min, then **bpib** (0.128 g, 0.25 mmol) dispersed in glycerol was added gradually, and the resulting mixture refluxed for 12 h. After cooling to room temperature, a dark-red precipitate was obtained by dropwise addition of aqueous NH$_4$PF$_6$ solution. The product was purified by column chromatography on alumina with acetonitrile-ethanol as eluent. Yield: 0.36 g (72%). ESI-MS (m/z, Fragment): 791.23 ([Ru$_2$(phen)$_4$(bipb)PF$_6$]$^{3+}$, [M-H]$^{2+}$), 719.25 ([Ru$_2$(phen)$_4$(bipb)]$^{4+}$, [M-2H]$^{2+}$), 478.96 ([Ru$_2$(phen)$_4$(bipb)]$^{4+}$, [M-H]$^{3+}$), 359.89 ([Ru$_2$(phen)$_4$(bipb)$_6$]$^{4+}$,[M]$^{4+}$). ^{1}H NMR (400 MHz, d$_6$-DMSO) δ (ppm): 9.04 (d, *J* =8.0 Hz, 4H), 8.77 (d, *J* =8.0 Hz, 8H), 8.49 (s, 4H), 8.39 (s, 8H), 8.13 (d, *J* =4.0 Hz, 8H), 7.81-7.76 (m, 12H), 7.67 (t, *J* =4.0 Hz, 4H). MALDI-TOF-MS (m/z, Fragment): 460.27 ([Ru(phen)$_2$]$^{2+}$, [M-H]$^+$), 515.44 (bipb, [M+H]$^+$), 577.40 ([Ru(phen)(ipb)]$^{2+}$, [M-H]$^+$), 974.72 ([Ru(phen)$_2$(bipb)]$^{2+}$, [M-H]$^+$).

Synthesis of [Ru$_2$(phen)$_4$(bdppz)](PF$_6$)$_4$ (Ru-bdppz-2) [3]

A solution of Ru(phen)$_2$Cl$_2$.2H$_2$O (0.284 g, 0.5 mmol) in glycerol was heated under nitrogen for 30 min, then **bdppz** (0.141 g, 0.25 mmol) dispersed in glycerol was added gradually, and the resulting mixture refluxed for 6 h. After cooling to room temperature, a dark-red precipitate was obtained by dropwise addition of aqueous NH$_4$PF$_6$ solution. The product was purified by column chromatography on alumina with acetonitrile-ethanol as eluent. Yield: 0.36 g (70%). ESI-MS (m/z, Fragment): 371.94 ([Ru$_2$(phen)$_4$(bdppz)]$^{4+}$, [M]$^{4+}$), 496.58 ([Ru$_2$(phen)$_4$(bdppz)]$^{4+}$, [M-H]$^{3+}$).^{1}H NMR (400 MHz, d$_6$-DMSO) δ (ppm): 9.66 (dd, J =4.0 Hz, 4H), 9.20 (s, 2H), 8.96 (d, J =8.0 Hz, 2H), 8.81(t, J =8.0 Hz, 8H), 8.74 (d, J =8.0 Hz, 2H), 8.42 (s, 8H), 8.31 (d, J =4.0 Hz, 4H), 8.23(t, J =4.0 Hz, 4H), 8.08 (d, J =4.0 Hz, 4H),7.96(dd, J$_1$ =8.0 Hz, J$_2$ =4.0 Hz, 4H), 7.85-7.77 (m, 8H). MALDI-TOF-MS (m/z, Fragment): 460.28 ([Ru(phen)$_2$]$^{2+}$, [M-H]$^+$), 842.57 ([Ru(phen)(bdppz)]$^{2+}$, [M-H]$^+$), 1020.72 ([Ru(phen)$_2$(bdppz)]$^{2+}$, [M-H]$^+$).

Synthesis of $Ru_n(phen)_n(bipb)_{n+1}](ClO_4)_{2n}$ (Ru-bipb-n)

A mixture of **bipb** (0.514 g, 1 mmol) and $Ru(phen)Cl_4$ (0.423 g, 1 mmol) were refluxed in 25 mL N,N-dimethylformamide for 6 h under nitrogen. After cooling to room temperature, a brown precipitate was obtained by dropwise addition of $NaClO_4$ solution. The residue was washed with deionized water and dried under vacuum. The crude product was refluxed in ethanol and acetonitrile for 2 h to remove soluble low-molecular-weight complex, following filtration, a brown power was obtained. Yield: 0.472 g. Element analysis: 51.90%; N, 13.88%, H, 2.73%. MALDI-TOF-MS (m/z, Fragment): 282.16 ($[Ru(phen)]^{2+}$, $[M-H]^+$), 317.03 ($[Ru(phen)Cl]^+$), 462.04 ($[Ru(phen)_2]^{2+}$, $[M-H]^+$), 476.60 ($[Ru(phen)(5\text{-}NH_2\text{-}phen)]^{2+}$, $[M-H]^+$), 496.98 ($[Ru(phen)_2Cl]^+$), 515.30 (bipb, $[M+H]^+$), 658.08 ($[Ru(phen)_2(5\text{-}NH_2\text{-}phen)]^{2+}$, $[M-H]^+$), 793.97 ($[Ru(phen)(bipb)]^{2+}$, $[M-H]^+$), 975.04 ($[Ru(phen)_2(bipb)]^{2+}$, $[M-H]^+$), 2026.71 ($[Ru_3(phen)(bipb)(bipbH_2)_2]^{6+}$, $[M-5H]^+$), 2105.02 ($[Ru_2(phen)_2(bipb)_2(bipbH_2)]^{4+}$, $[M-3H]^+$), 2204.84 ($[Ru_3(phen)_2(bipb)_2(bipbH_2)]^{6+}$, $[M-5H]^+$), 2349.43 ($[Ru_3(phen)_2(bipb)_3Cl_4]^{2+}$, $[M-H]^+$), 2999.09 ($[Ru_4(phen)_3(bipb)_4]^{8+}$, $[M-7H]^+$), 3791.88 ($[Ru_5(phen)_4(bipb)_5]^{10+}$, $[M-9H]^+$), 4585.87 ($[Ru_6(phen)_5(bipb)_6]^{12+}$, $[M-11H]^+$).

Synthesis of $[Ru_n(phen)_n(bdppz)_{n+1}](ClO_4)_{2n}$ (Ru-bdppz-n)

A mixture of **bdppz** (0.563 g, 1 mmol) and $Ru(phen)Cl_4$ (0.423 g, 1 mmol) were refluxed in 25 mL N,N-dimethylformamide for 6 h under nitrogen. After cooling to room temperature, a black precipitate was obtained by dropwise addition of $NaClO_4$ solution. The residue was washed with deionized water and dried under vacuum. The crude product was refluxed in ethanol and acetonitrile for 2 h to remove soluble low-molecular-weight complex, following filtration, a black power was obtained. Yield: 0.62 g. Element analysis: 54.23%; N, 13.36%, H, 2.50%. MALDI-TOF-MS (Fragment, m/z): 282.16 ($[Ru(phen)]^{2+}$, $[M-H]^+$), 317.04 ($[Ru(phen)Cl]^+$), 462.02 ($[Ru(phen)_2]^{2+}$, 496.98 ($[Ru(phen)_2Cl]^+$), 563.11 (bdppz, $[M+H]^+$), 841.99 ($[Ru(phen)(bdppz)]^{2+}$, $[M-H]^+$), 878.97 ($[Ru(phen)(bdppz)Cl]^+$), 1224.02 ($[Ru(bdppz)_2]^{2+}$, $[M-H]^+$), 2073.59 ($[Ru_2(phen)(bdppzH_2)_3]^{4+}$, $[M-3H]^+$), 2108.46 ($[Ru_2(phen)(bdppzH_2)_3Cl]^{3+}$, $[M-2H]^+$), 2167.59 ($[Ru_3(phen)(bdppz)_3]^{6+}$, $[M-5H]^+$), 2201.50 ($[Ru_3(phen)(bdppz)_3Cl]^{5+}$, $[M-4H]^+$), 2314.63 ($[Ru_3(phen)(bdppz)_2(bdppzH_2)Cl_4]^{2+}$, $[M-H]^+$), 2346.69 ($[Ru_3(phen)(bdppz)_3Cl_5]^+$), 2698.59 ($[Ru_4(phen)_3(bdppz)_3Cl_2]^{6+}$, $[M-5H]^+$), 3468.77 ($[Ru_5(phen)_4(bdppz)_4]^{10+}$, $[M-9H]^+$), 4312.08 ($[Ru_6(phen)_5(bdppz)_5]^{12+}$, $[M-11H]^+$).

2. Figures and Legends

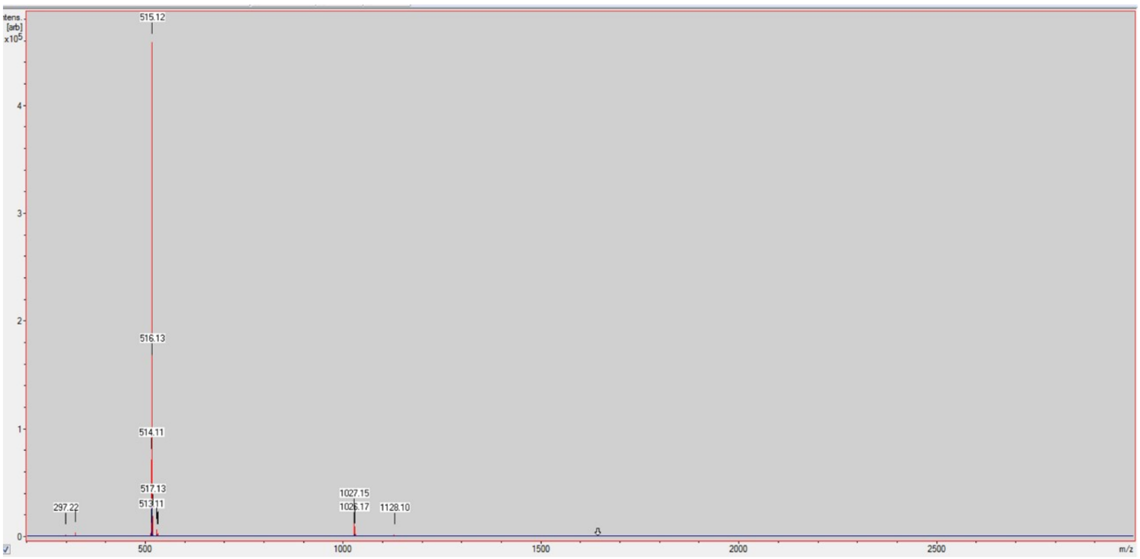

Figure S1. MALDI-TOF-MS spectra of the ligand **bipb**

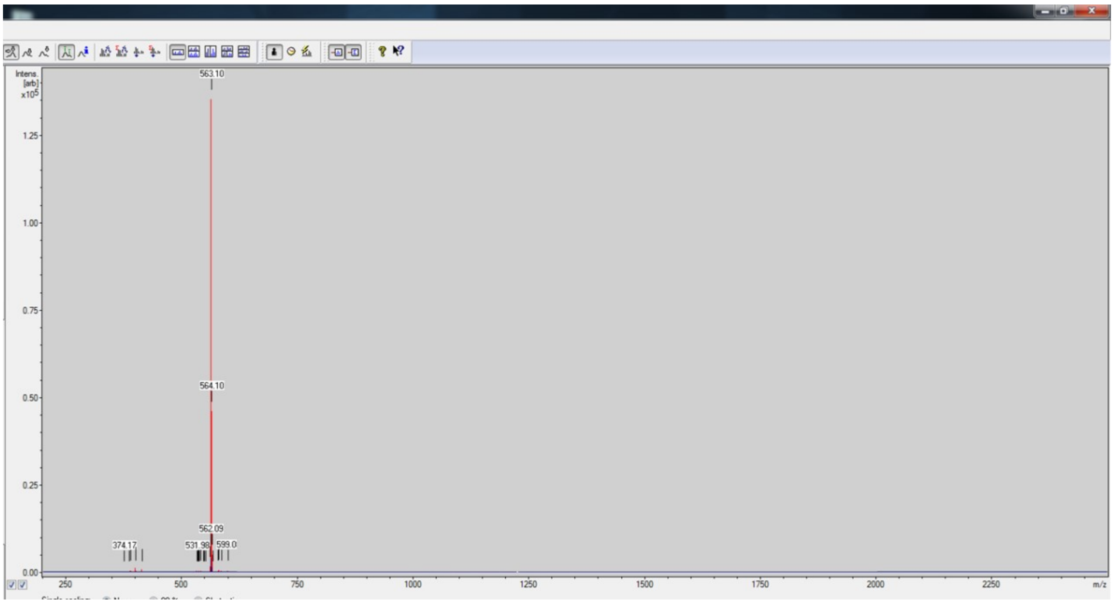

Figure S2. MALDI-TOF-MS spectra of the ligand **bdppz**

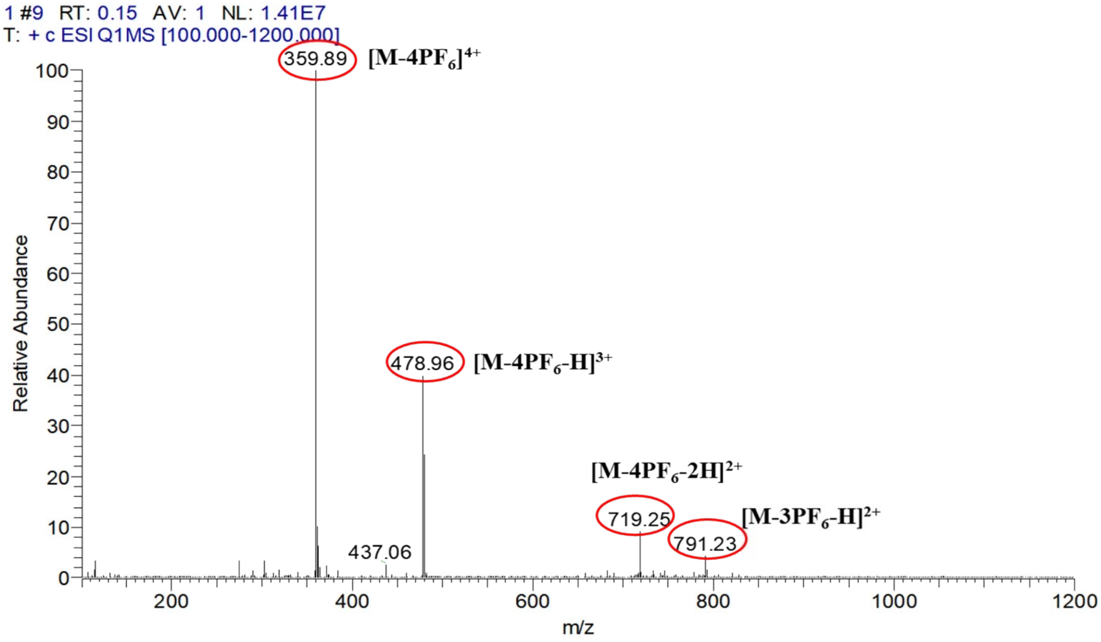

Figure S3. ESI-MS spectra of the complex **Ru-bipb-2**.

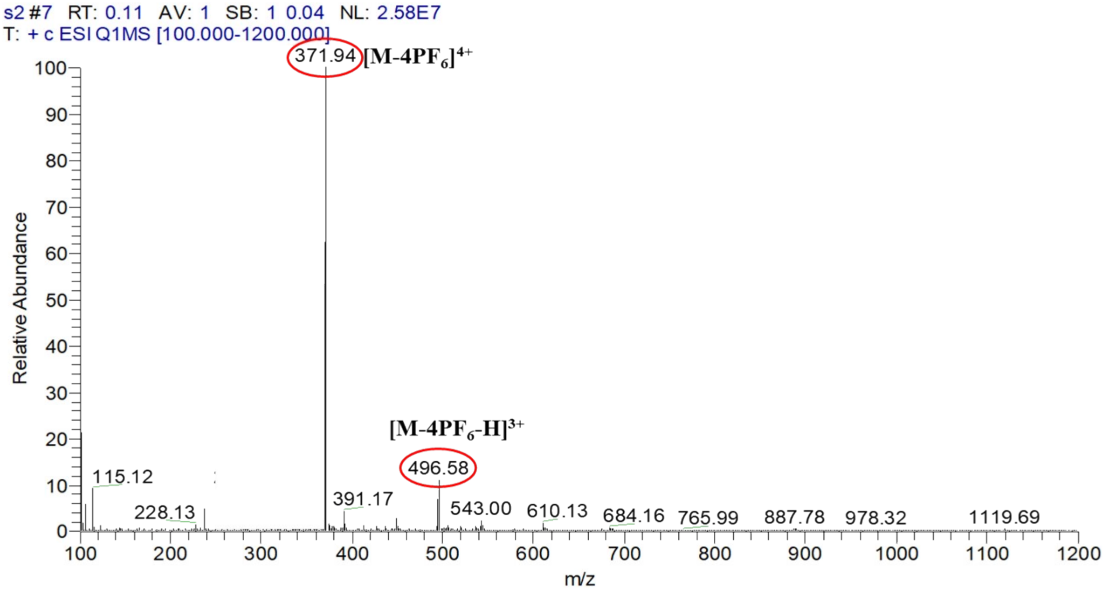

Figure S4. ESI-MS spectra of the complex **Ru-bdppz-2**.

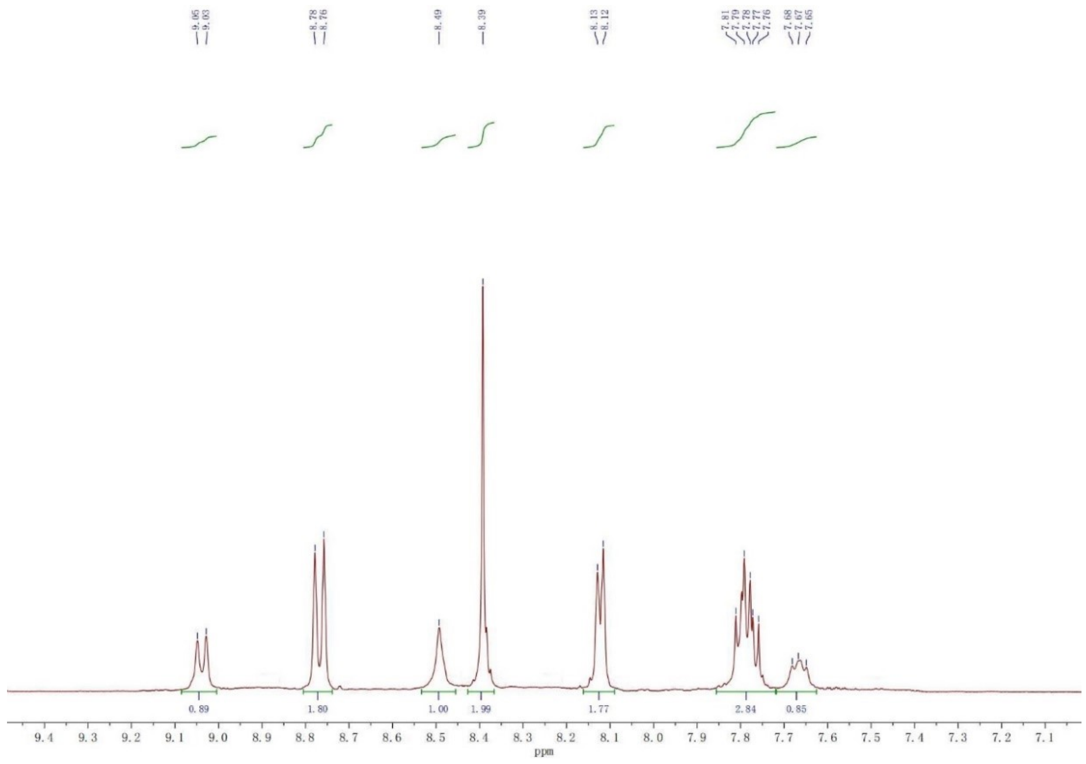

Figure S5. ^{1}H NMR spectra of the complex **Ru-bipb-2**.

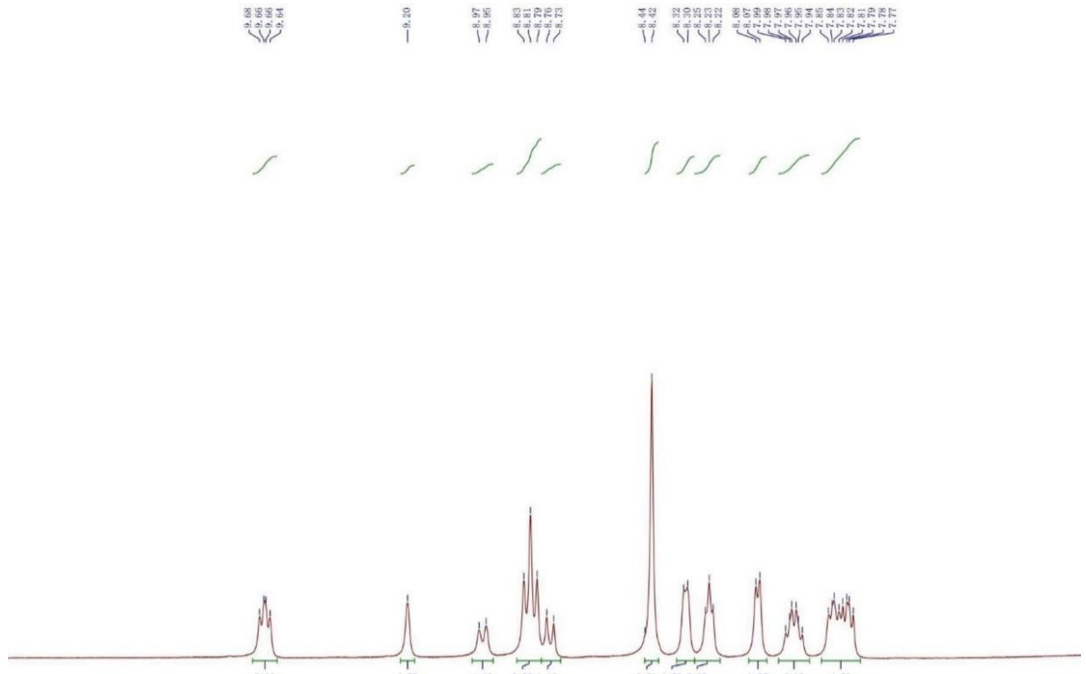

Figure S6. ^{1}H NMR spectra of the complex **Ru-bdppz-2**.

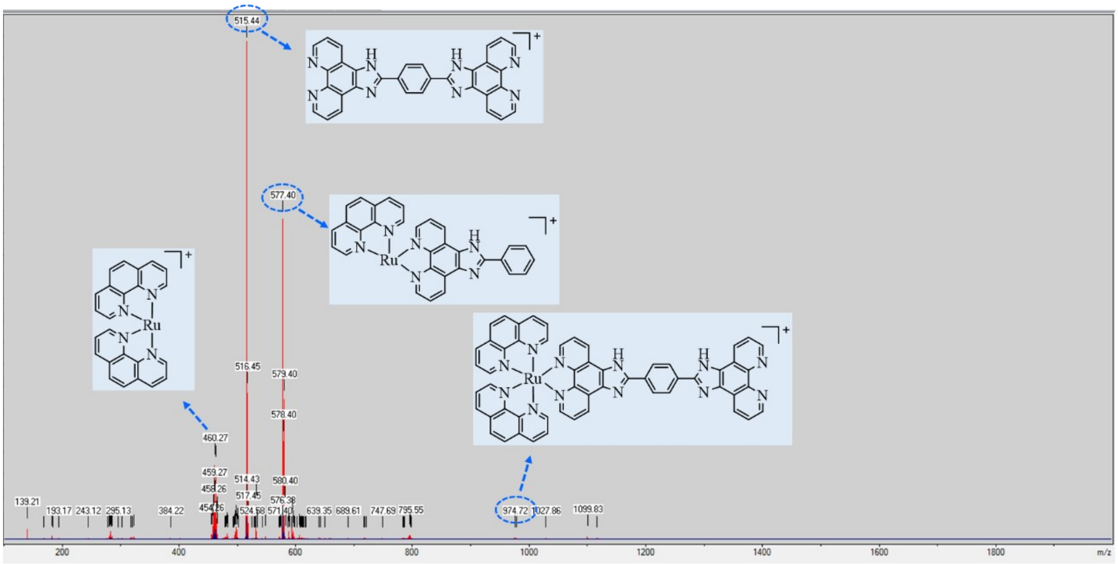

Figure S7. MALDI-TOF-MS spectra of **Ru-bipb-2**.

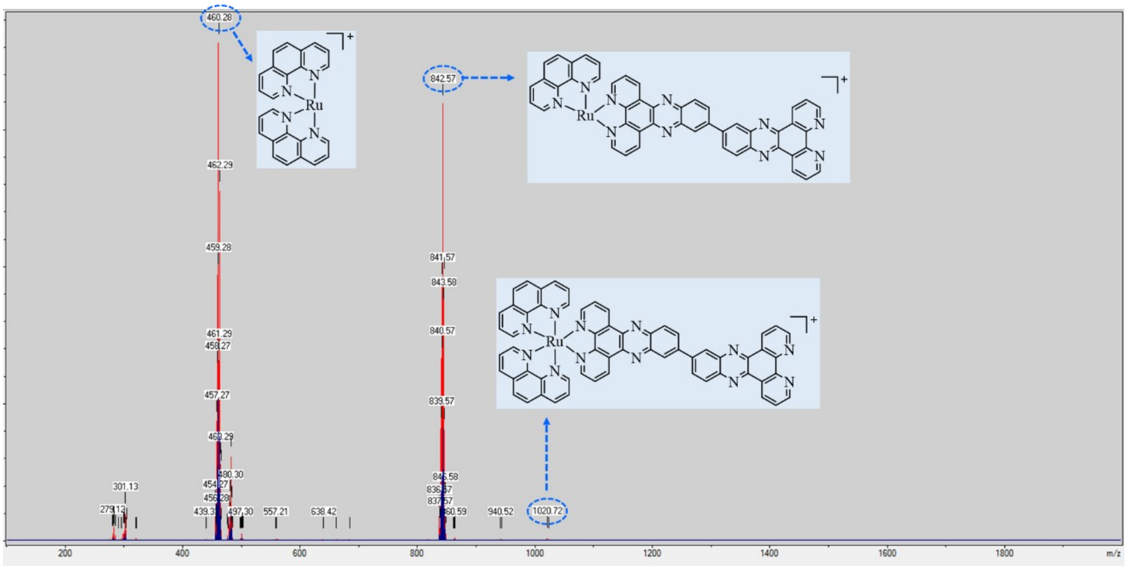

Figure S8. MALDI-TOF-MS spectra of **Ru-bdppz-2**.

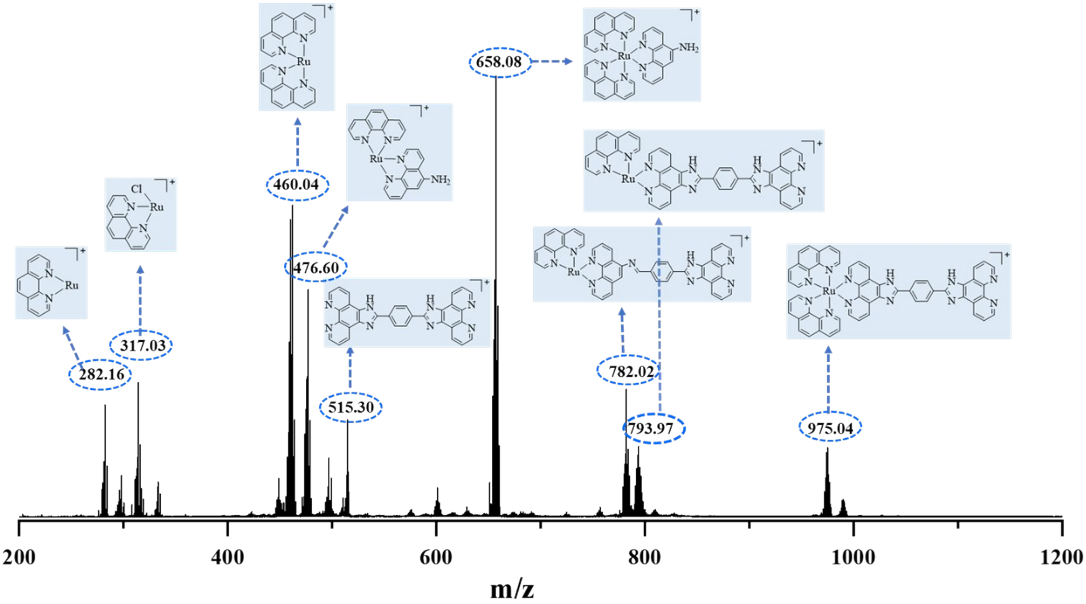

Figure S9. MALDI-TOF-MS spectra of **Ru-bipb-n** in the 200-2000 m/z range.

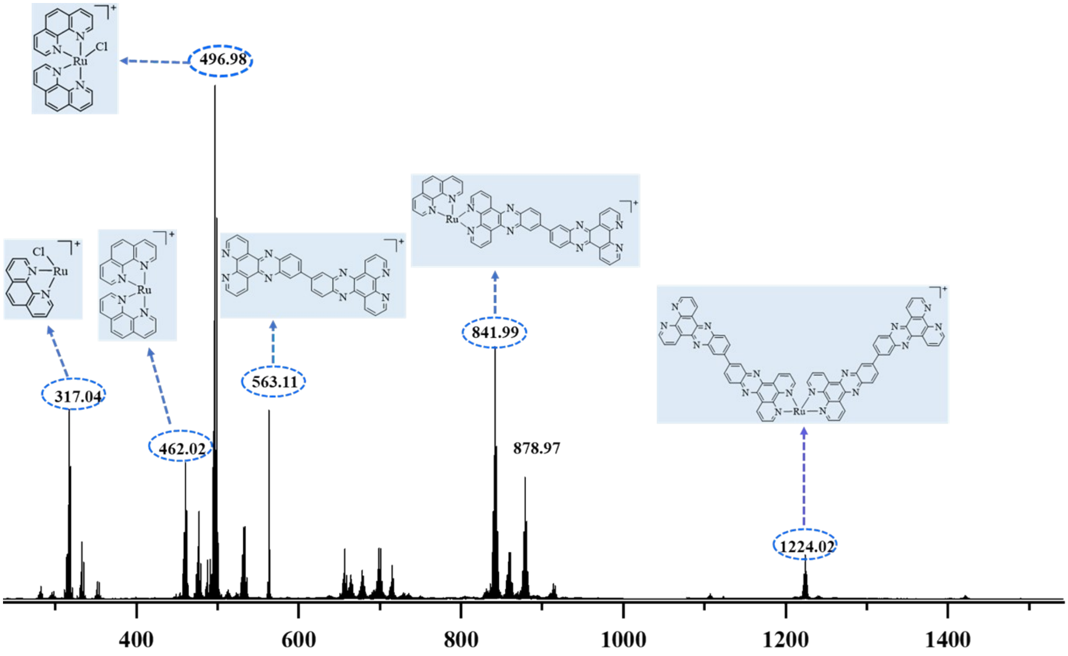

Figure S10. MALDI-TOF-MS spectra of **Ru-bdppz-n** in the 200-2000 m/z range.

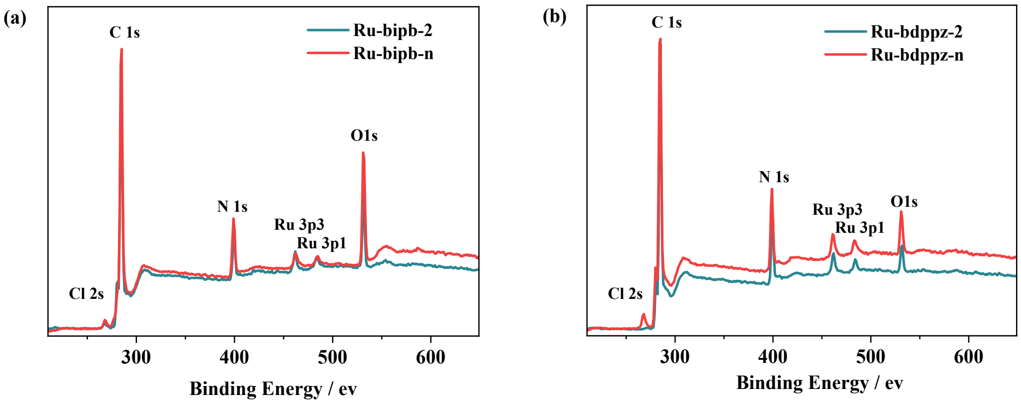

Figure S11. XPS survey spectra of **Ru-bipb-n** (a) and **Ru-bdppz-n** (b).

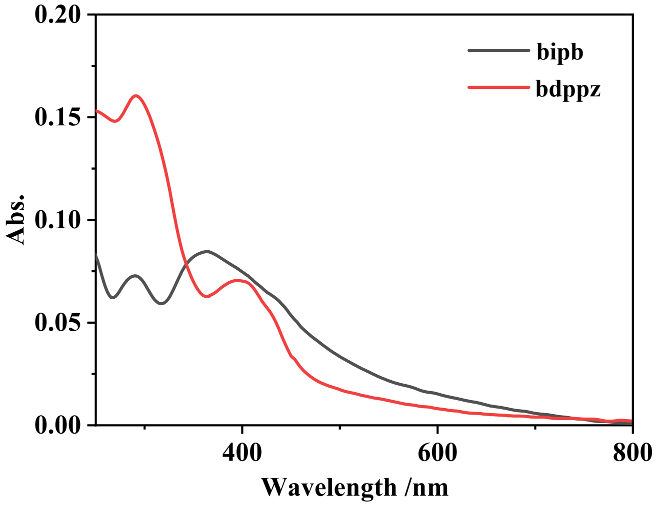

Figure S12. Absorption spectra of the ligands **bipb** and **bdppz** (10 μM) in H_2O.

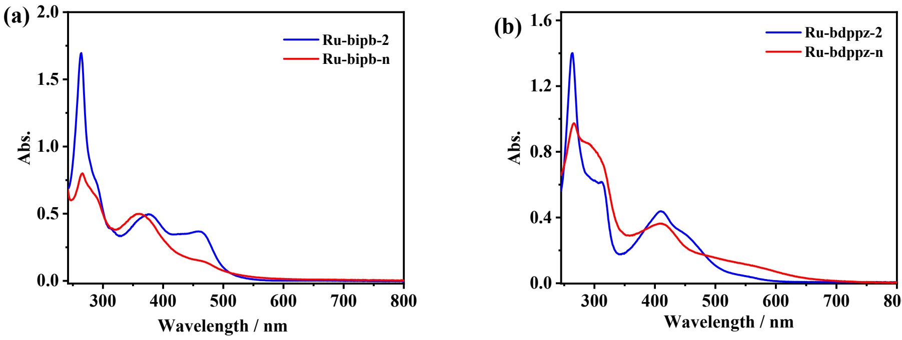

Figure S13. Absorption spectra of **Ru-bipb-2** (a, blue line), **Ru-bipb-n** (a, red line), **Ru-bdppz-2** (b, blue line) and **Ru-bdppz-n** (b, red line) (20 μg/mL) in H_2O.

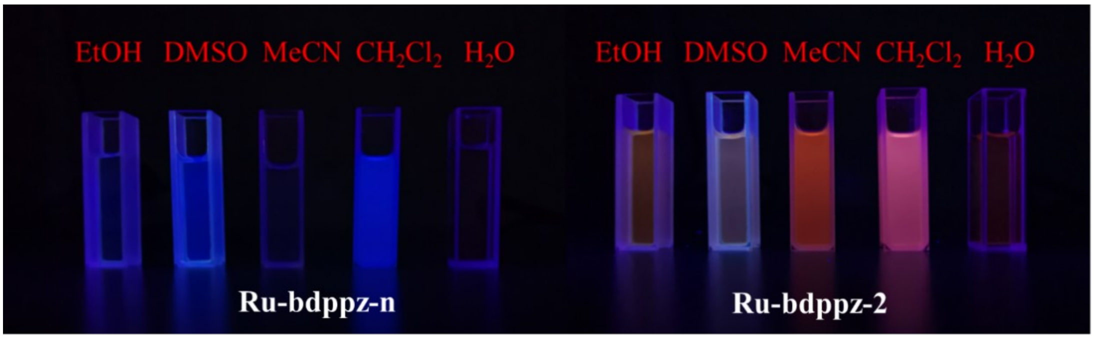

Figure S14. Emission image of **Ru-bdppz-n** (20 μg/mL) (left) and **Ru-bdppz-2** (20 μg/mL) (right) in various solvents under UV light irradiation (365 nm).

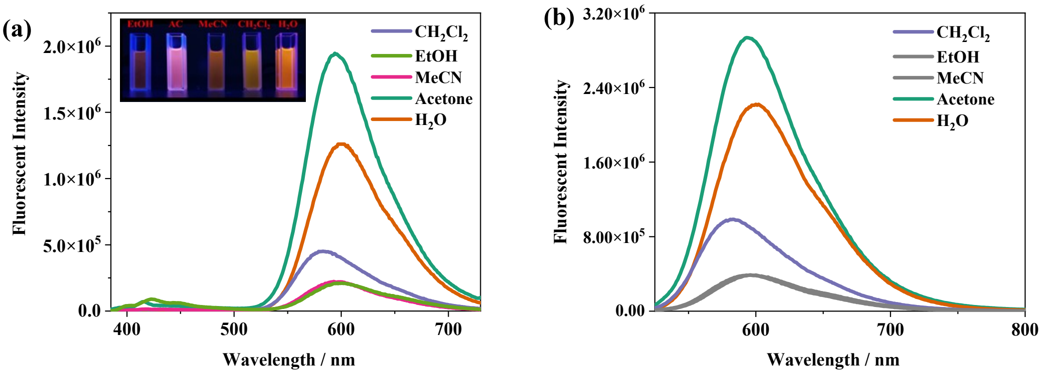

Figure S15. Emission spectra of **Ru-bipb-2** (10 μg/mL) in various solvents under excitation at 370 nm (a) and 460 nm (b). Inset: Fluorescence image of **Ru-bipb-2**.

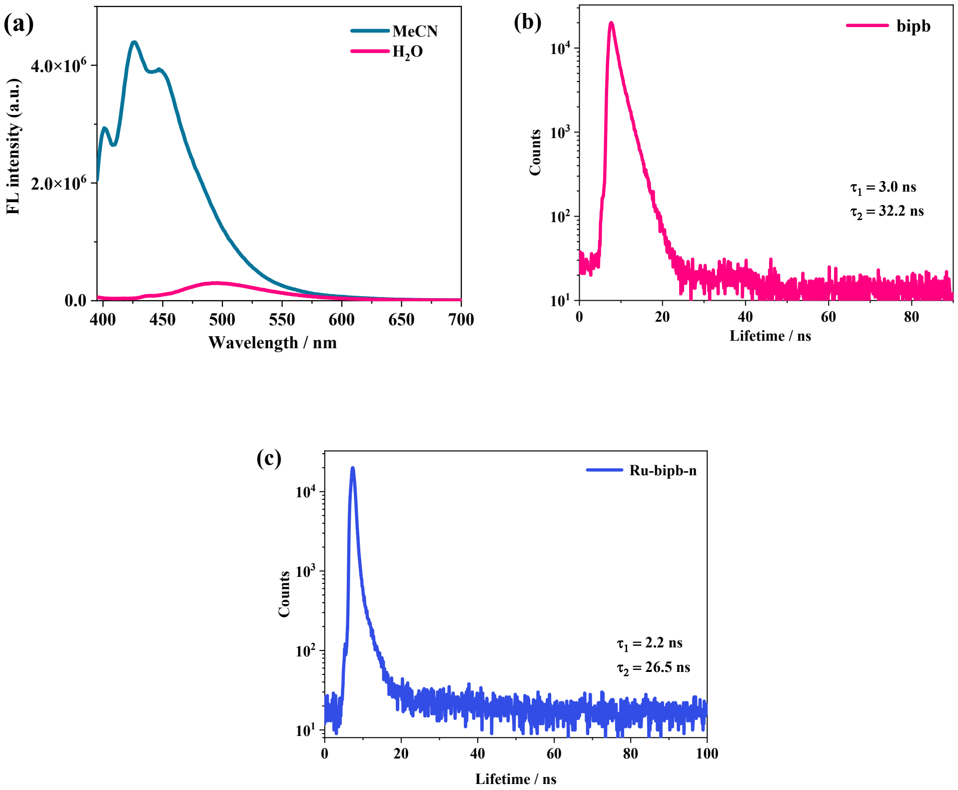

Figure S16. (a) Fluorescence spectra of the ligand **bipb** (10 μg/mL) in acetonitrile and H_2O under excitation at 370 nm. (b-c) Fluorescence decay curve of **bipb** (b) and **Ru-bipb-n** (c) in H_2O, λ_{ex} = 370 nm, λ_{em} = 480 nm.

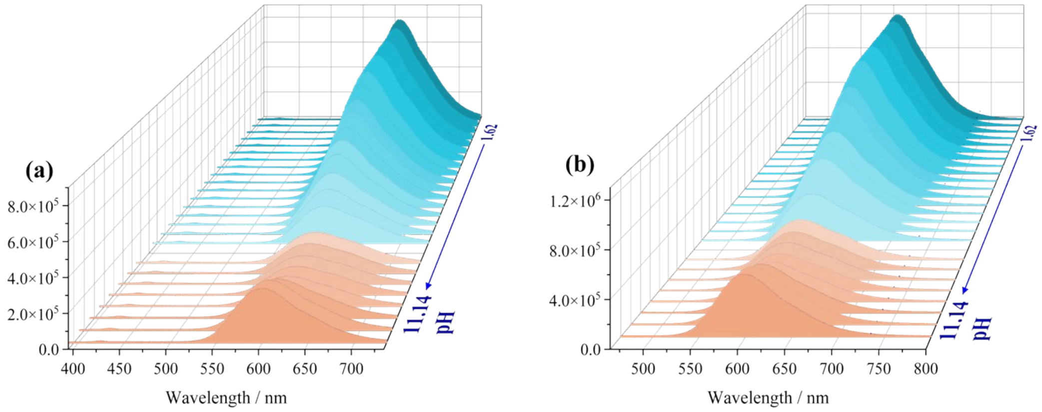

Figure S17. Emission spectra **Ru-bipb-2** (10 μg/mL) as a function of pH under the excitation of 370 nm (a) and 460 nm (b).

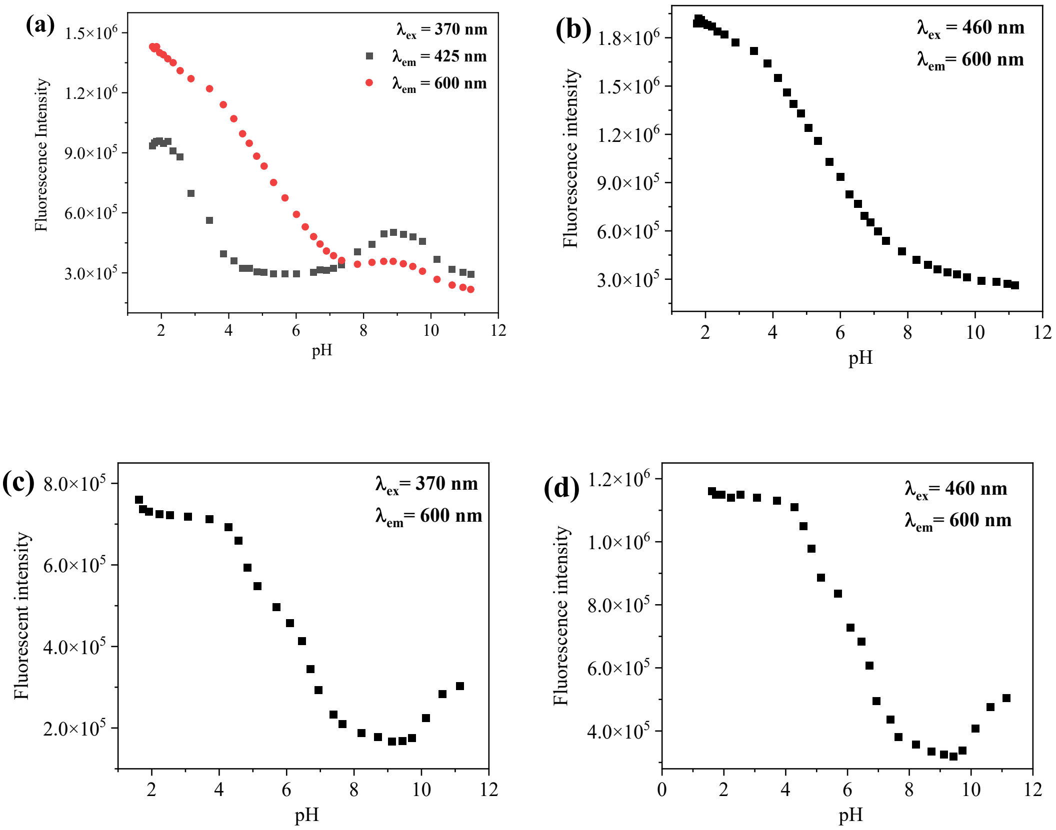

Figure S18. The emission intensity **Ru-bipb-n** (10 μg/mL) (a, b) and **Ru-bipb-2** (10 μg/mL) (c, d) as a function of pH with excitation of 370 nm (a, c) and 460 nm (b, d).

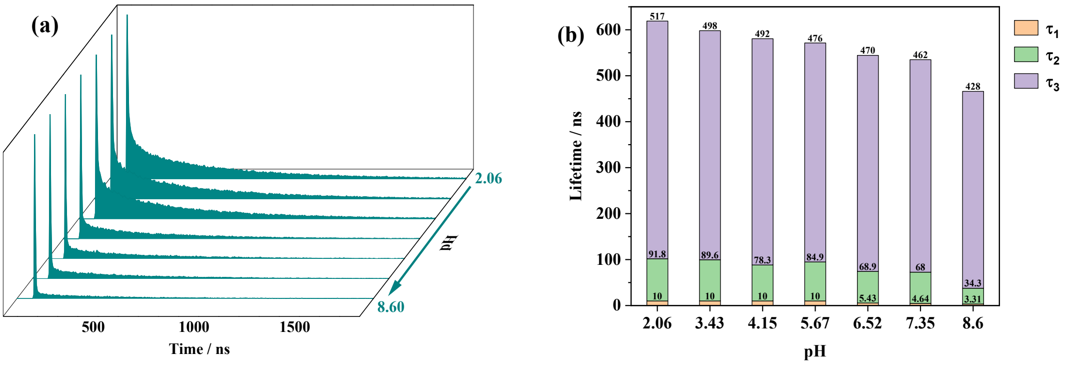

Figure S19. (a) Fluorescence decay curves of **Ru-bipb-n** in different pH solutions. (b) Fluorescence lifetime changes of **Ru-bipb-n** with the variation of pH. λ_{ex} = 370 nm, λ_{em} = 600 nm.

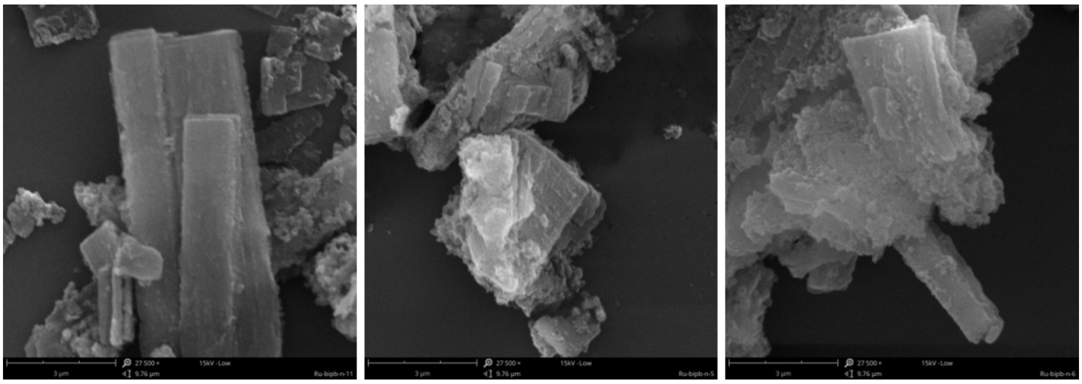

Figure S20. The SEM image of **Ru-bipb-n** under neutral (pH=7.0, middle), acidic (pH=1.8, left), and alkaline (pH=12.0, right) conditions.

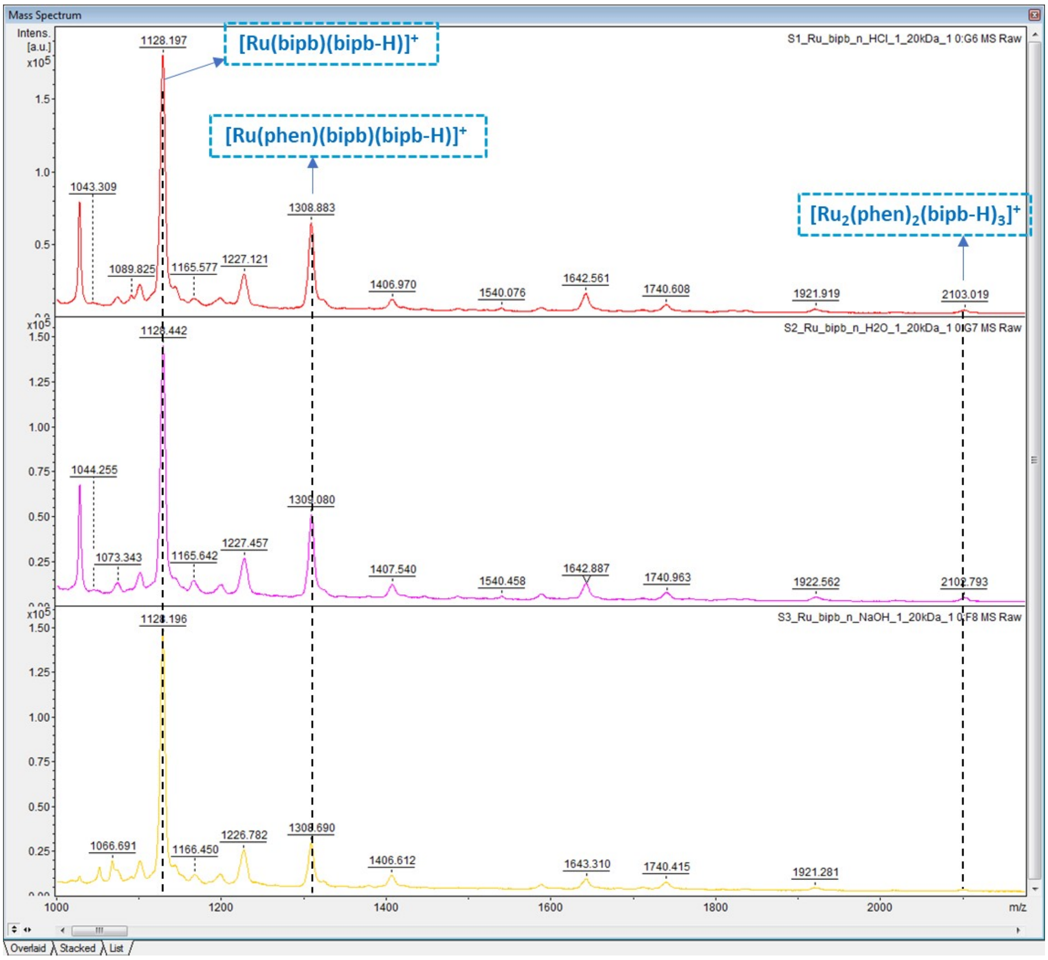

Figure S21. The MALDI-TOF-MS spectra of **Ru-bipb-n** under neutral (pH=7.0, middle), acidic (pH=1.8, left), and alkaline (pH=12.0, right) conditions within the m/z range 1000-2500.

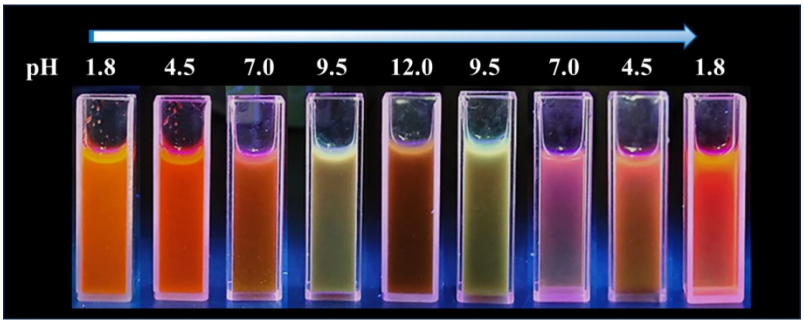

Figure S22. The reversibility of pH response behavior of **Ru-bipb-n** under acidic and alkaline conditions.

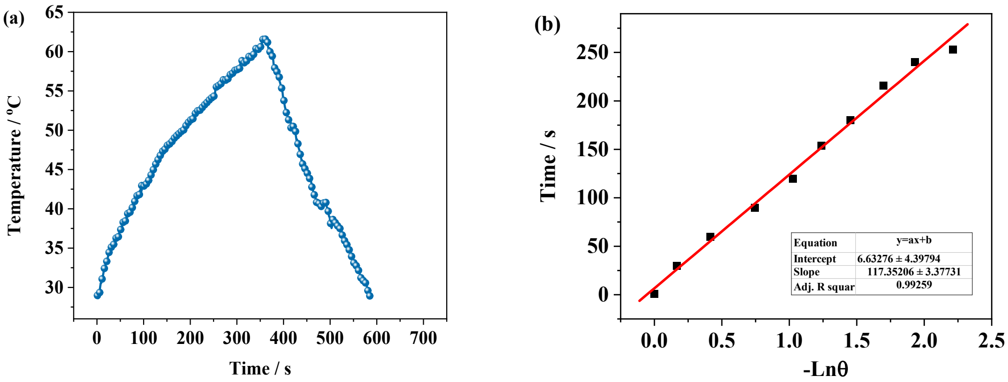

Figure S23. (a) The heating and cooling curve of **Ru-bdppz-n** after the irradiation of 808 nm laser (1.0 mg/mL in H_2O, 1.5 W/cm^2) and (b) its corresponding time-lnθ linear curve.

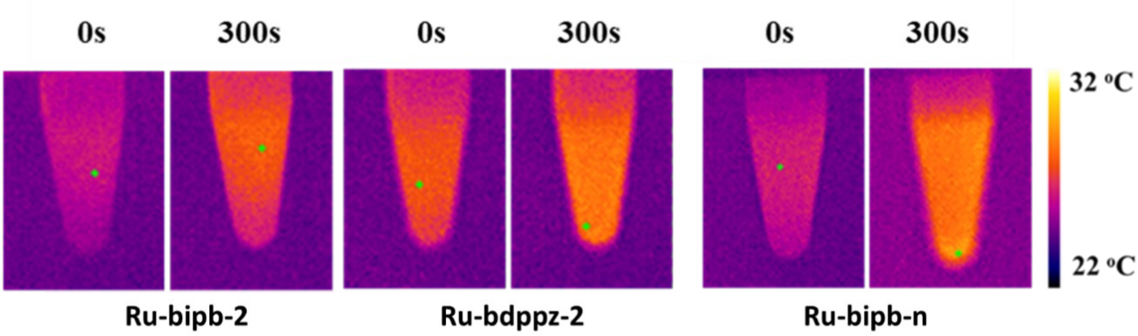

Figure S24. IR thermal images of **Ru-bipb-2**, **Ru-bdppz-2**, and **Ru-bipb-n** dispersion under 808-nm laser irradiation (1.0 mg/mL, 1.5 W/cm^2).

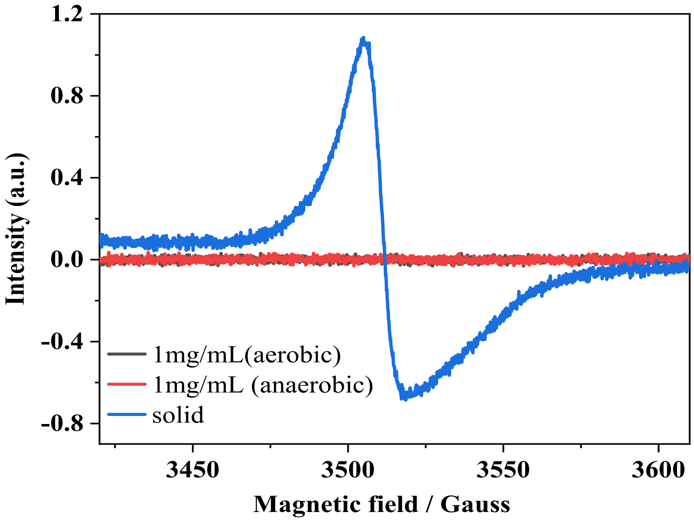

Figure S25. EPR spectrum of **Ru-bdppz-n** dispersion in H_2O (1 mg/mL) under aerobic and anaerobic conditions.

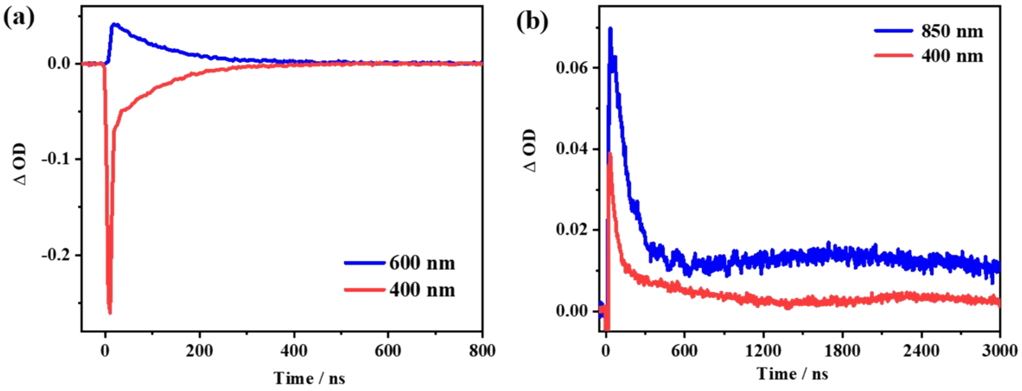

Figure S26. Time profiles of the transient bands of **Ru-bdppz-2** at 400 and 600 nm (a) and **Ru-bdppz-n** at 400 and 800 nm (b) in acetonitrile (10 μg/mL) with light excitation at 355 nm.

Table S1. Emission lifetime of **Ru-bipb-n** at different pH.

pH	τ_1/ns	Rel%	τ_2/ns	Rel%	τ_3/ns	Rel%	X^2
2.06	10.00	1.52%	91.84	8.76%	517.06	89.72%	1.027
3.43	10.00	2.29%	89.57	9.28%	498.40	88.43%	1.005
4.15	10.00	0.37%	78.30	7.80%	492.18	91.84%	1.045
5.67	10.00	2.16%	84.90	7.85%	476.47	89.99%	1.011
6.52	5.44	2.27%	68.87	7.23%	469.96	90.50%	1.022
7.35	4.63	3.28%	67.99	5.62%	462.23	91.10%	0.995
8.60	3.31	5.77%	34.30	4.77%	428.35	89.47%	0.997
Testing condition: λ_{ex} = 370 nm, λ_{em} = 600 nm, t = 25 ^oC (t = temperature), solvent: H_2O							

Table S2. Photothermal properties of **Ru-bdppz-n** and reported materials

No	Compound	Light source (nm)	Intensity (Wcm^{-2})	Temperature at 5s	Temperature at quilibrium	reference
1	**Ru-bdppz-n**	808	0.1	66.9	68.2	This work
			0.2	89.4	92.4	
			0.3	114.8	124.6	
			0.4	155.2	161.9	
			0.5	177	189.7	
			0.6	205.1	220	
2	CF	808	0.142	46	51	[7]
			0.241	70	75	
			0.276	78	82	
3	CR-TPE-T	808	0.2	32	35	[8]
			0.4	50	58	
			0.6	70	76	
			0.8	92	100	
4	Tri-PMDI -TTF	808	0.7	20	80	[9]
5	DTC	808	0.7	30	71.3	[6]
6	Fe-MIL-NH_2	300-650	0.5	100	143	[10, 11]
7	UiO-66-NH_2	300-650	0.5	100	149	[10, 11]
8	ZIF-67	300-650	0.5	100	127	[10, 11]
9	CPO-27-Ni	300-650	0.5	120	166.7	[10, 11]
10	CPO-27-Zn	300-650	0.5	90	145	[10, 11]
11	NKU-123	808	1.0	215	215	[12]

References

1. Krause, R. A., Synthesis of mixed complexes of ruthenium(II) with 2,2′-dipyridyl. *Inorg. Chim. Acta.* **1977,** *22*, 209-213.
2. Chao, H.; Li, R.-H.; Jiang, C.-W.; Li, H.; Ji, L.-N.; Li, X.-Y., Mono-, di- and tetra-nuclear ruthenium(II) complexes containing 2,2′-p-phenylenebis(imidazo[4,5-f]phenanthroline): synthesis, characterization and third-order non-linear optical properties. *Dalton Trans.* **2001,** (12), 1920-1926.
3. Bilakhiya, A. K.; Tyagi, B.; Paul, P.; Natarajan, P., Di- and tetranuclear ruthenium(II) and/or osmium(II) complexes of polypyridyl ligands bridged by a fully conjugated aromatic spacer: synthesis, characterization, and electrochemical and photophysical studies. *Inorg. Chem.* **2002,** *41* (15), 3830-42.
4. Han, M.; Kim, B.; Lim, H.; Jang, H.; Kim, E., Transparent Photothermal Heaters from a Soluble NIR-Absorbing Diimmonium Salt. *Adv. Mater.* **2020,** *32* (1), e1905096.
5. Kim, B.; Han, M.; Kim, E., Photothermally powered conductive films for absorber-free solar thermoelectric harvesting. *J. Mater. Chem. A* **2019,** *7* (5), 2066-2074.
6. Wang, Y.; Zhu, W.; Du, W.; Liu, X.; Zhang, X.; Dong, H.; Hu, W., Cocrystals Strategy towards Materials for Near-Infrared Photothermal Conversion and Imaging. *Angew. Chem. Int. Ed. Engl.* **2018,** *57* (15), 3963-3967.
7. Zhao, Y. D.; Han, J.; Chen, Y.; Su, Y.; Cao, Y. M.; Wu, B.; Yu, S. M.; Li, M.-D.; Wang, Z.; Zheng, M.; Zhuo, M.-P.; Liao, L.-S., Organic Charge-Transfer Cocrystals toward Large-Area Nanofiber Membrane for Photothermal Conversion and Imaging. *ACS Nano* **2022,** *16* (9), 15000-15007.
8. Chen, G.; Sun, J.; Peng, Q.; Sun, Q.; Wang, G.; Cai, Y.; Gu, X.; Shuai, Z.; Tang, B. Z., Biradical-Featured Stable Organic-Small-Molecule Photothermal Materials for Highly Efficient Solar-Driven Water Evaporation. *Adv. Mater.* **2020,** *32* (29), 1908537.
9. Wang, D.; Kan, X.; Wu, C.; Gong, Y.; Guo, G.; Liang, T.; Wang, L.; Li, Z.; Zhao, Y., Charge transfer co-crystals based on donor–acceptor interactions for near-infrared photothermal conversion. *Chem. Commun.* **2020,** *56* (39), 5223-5226.
10. Su, Y.; Chen, Z.; Tang, X.; Xu, H.; Zhang, Y.; Gu, C., Design of Persistent and Stable Porous Radical Polymers by Electronic Isolation Strategy. *Angew. Chem. Int. Ed. Engl.* **2021,** *60* (46), 24424-24429.
11. Espín, J.; Garzón-Tovar, L.; Carné-Sánchez, A.; Imaz, I.; Maspoch, D., Photothermal Activation of Metal-Organic Frameworks Using a UV-Vis Light Source. *ACS Appl. Mater. Interfaces* **2018,** *10* (11), 9555-9562.
12. Lan, W.; Gou, X.; Wu, Y.; Liu, N.; Lu, L.; Cheng, P.; Shi, W., The Influence of Light-Generated Radicals for Highly Efficient Solar-Thermal Conversion in an Ultra-Stable 2D Metal-Organic Assembly. *Angew. Chem. Int. Ed. Engl.* **2024,** *63* (n/a), e202401766.